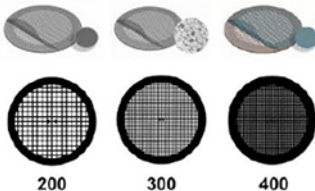# Nanocharacterization by TEM and AFM

We offer a wide range of TEM and AFM tools, from TEM grids and finders to AFM substrates and grippers.

Available in a wide variety of designs and materials to support your work, select from a broad range of mesh sizes, specimen supporting films, and materials that perfectly suit the conditions of your TEM analysis.
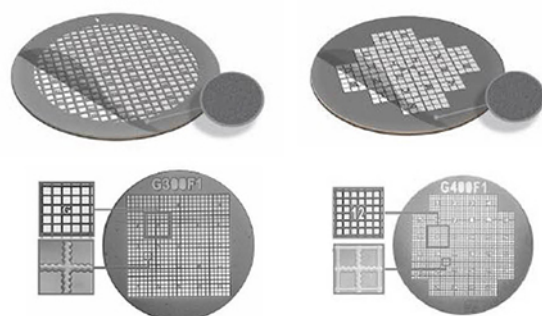
TEM grid specifications:

Material	Mesh Size and Shape	Film Specifications
• Cu • Ni • Au • Mo • Cu/Pd	• Square or hexagonal • Single-hole grid (75 mm or 100 mm) • 100 • 150 • 200 • 300 • 400	• None • Continuous formvar film (thicknesses: 5-6 nm, 10 nm) • Lacey carbon film (average hole sizes: 50 nm, 100 nm, 150 nm, 100 mm, 150 mm) • Continuous amorphous carbon film (thicknesses: 10 nm, 20-30 nm) • Continuous formvar/carbon film (thickness: 10nm formvar and 1nm carbon)

200   300   400

TEM finder grid specifications:

Material	Mesh Size	Film Specifications
• Cu • Ni • Au	• 135 • 200 • 300 • 400	• None • Continuous amorphous carbon film (thicknesses: 3-4 nm, 10 nm, 20-30 nm)

Supporting Tools for Nanomaterial Characterization

Our comprehensive range of supporting materials for nanomaterial characterization includes tweezers (sharp tip, disc gripper for AFM), TEM window grids (various thicknesses, 1 or 9 windows), a magnetic pick-up tool, a grid storage box, cryo-capsules, lift-out grids (Cu or Mo), AFM substrates (various dimensions), and much more.

Explore our complete range of TEM grids on:
SigmaAldrich.com/nanocharacterization

The Life Science business of Merck operates as MilliporeSigma in the U.S. and Canada.

Sigma-Aldrich®

Lab & Production Materials

Influence of the Current Density on the Interfacial Reactivity of Layered Oxide Cathodes for Sodium-Ion Batteries

Maider Zarrabeitia,* Teófilo Rojo, Stefano Passerini, and Miguel Ángel Muñoz-Márquez*

The full commercialization of sodium-ion batteries (SIBs) is still hindered by their lower electrochemical performance and higher cost ($\$ W^{-1} h^{-1}$) with respect to lithium-ion batteries. Understanding the electrode–electrolyte interphase formation in both electrodes (anode and cathode) is crucial to increase the cell performance and, ultimately, reduce the cost. Herein, a step forward regarding the study of the cathode–electrolyte interphase (CEI) by means of X-ray photoelectron spectroscopy (XPS) has been carried out by correlating the formation of the CEI on the P2-$Na_{0.67}Mn_{0.8}Ti_{0.2}O_2$ layered oxide cathode with the cycling rate. The results reveal that the applied current density affects the concentration of the formed interphase species, as well as the thickness of CEI, but not its chemistry, indicating that the electrode–electrolyte interfacial reactivity is mainly driven by thermodynamic factors.

1. Introduction

Sodium-ion batteries (SIBs) are considered the most promising technology to develop large-scale stationary applications, partially releasing the existing pressure on lithium-ion battery (LIB) production.[1] Since 2013, several SIB demonstrators have been developed and some are also commercial,[2–5] however, with no relevance in terms of market share, yet. A few industrial actions have been recently initiated, namely, the first high-energy SIBs order placed by the electrical engineering group ICM Australia to Faradion Ltd. (UK) for the commercialization of sodium-ion technology in the Australian market,[6] as well as the announcement of Contemporary Amperex Technology Co Ltd. (CATL). The latter company announced the development of commercial SIBs by 2023.[7]

Up to date, the commercialization of SIBs has been hindered by their lower electrochemical performance and higher cost (0.14 $\$ W^{-1} h^{-1}$ vs 0.11 $\$ W^{-1} h^{-1}$) with respect to LIBs.[8] However, SIBs can be made as competitive and sustainable electrochemical energy storage devices, not only by optimizing their active/inactive materials and components,[9] but also by understanding and controlling the relevant interfaces and interphases in the cell. However, intensive studies have been performed focused on the development and optimization of the electroactive materials (cathode, anode, and electrolyte)[1] so far, while fewer efforts have been directed toward the understanding of the electrode–electrolyte interphases, known as the solid–electrolyte interphase (SEI) on the negative electrode surface[10] and the cathode–electrolyte interphase (CEI) on the positive electrode.[11]

The SEI/CEI understanding, not only in terms of properties but also formation mechanism, is crucial because these interphases affect the overall battery performance in terms of power capability, Coulombic efficiency, irreversible capacity, long-term stability, and safety. In fact, the optimum electrode–electrolyte formulation enabling the formation of a stable SEI on the graphite electrode surface was the key for LIB commercialization.[12,13]

The SEI/CEI behaves as a passivation layer protecting the electrode materials from further decomposition reactions. For this reason, the SEI/CEI layers must be homogenous, uniform, and stable, and, ideally, it should prevent the electron conduction while allowing only the ionic transport, hence hindering further electrode–electrolyte reactions. Finally, the presence of the SEI/CEI should not reduce the overall electrochemical performance of the cell.[8]

M. Zarrabeitia, M. Á. Muñoz-Márquez[+]
Centre for Cooperative Research on Alternative Energies (CIC energiGUNE)
Basque Research and Technology Alliance (BRTA)
Alava Technology Park, Albert Einstein 48, 01510 Vitoria-Gasteiz, Spain
E-mail: maider.ipina@kit.edu; miguel.munoz@unicam.it

M. Zarrabeitia, S. Passerini
Helmholtz Institute Ulm (HIU)
Helmholtzstrasse 11, 89081 Karlsruhe, Germany

M. Zarrabeitia, S. Passerini
Karlsruhe Institute of Technology (KIT)
P.O. Box 3640, 76021 Karlsruhe, Germany

T. Rojo
Departamento de Química Inorgánica
Universidad del País Vasco UPV/EHU
P.O. Box 664, 48080 Bilbao, Spain

The knowledge of SIB interfaces and interphases is still limited, particularly if compared with the existing literature on LIB interfaces and interphases. In fact, a few investigations have been reported on the sodium-based negative electrode interfaces and interphases,[14–23] while even fewer studies can be found for the positive electrodes of SIBs.[24–27] One of the reasons for the impossibility to transfer the acquired knowledge on LIB electrode–electrolyte interphases directly to SIBs is due to the differences in the SEI/CEI properties.[28,29] Among such differences, the solubility of the sodium-based species upon electrochemical cycling[30] is one of the main parameters related to the poor long-term stability and electrochemical performance of SIBs.[17] Another critical difference is related to the SEI/CEI formation mechanisms, while usually organic-rich SEI is formed in lithium-based systems, an inorganic-rich SEI is found in SIBs.[14] Therefore, the understanding of the SEI/CEI formation, typically occurring during the first cycles due to reduction/oxidation reactions of the electrolyte, is of paramount importance for the SIB performance to approach the level of LIBs.

In the past years, there has been an increasing interest in the study of SIBs SEI/CEI chemistry and stability, including the correlation of the interphase properties with the electrochemical performance of the cells.[28,29] Nonetheless, additional efforts should be carried out in this field to reach the necessary improvements for boosting the commercialization of SIBs. Currently, the electrode–electrolyte interphase studies have been focused on the effect of electrode and electrolyte characteristics,[14–27] such as the electrolyte formulation, the coating of the electroactive material, and the integration of interlayers;[8,28,29] not considering other crucial parameters such as the applied current density or operating temperature. Indeed, cycling protocols at low current densities are typically applied to ensure the proper formation of the SEI, e.g., on hard carbon anodes, during the so-called formation cycles.[31] However, cycling protocols employing low current densities are time- and cost-consuming, involving up to 10% of the manpower and operation hours.[32] Therefore, the possibility of creating good passivation SEI/CEI at high current densities is highly appreciated by battery manufacturers. Nevertheless, to the best of our knowledge, the correlation between the SEI/CEI and applied current density in sodium-based intercalation materials has not been studied yet.

In this work, the CEI chemical composition, along with the estimation of its thickness, have been investigated for the electrochemically active P2-$Na_{0.67}Mn_{0.8}Ti_{0.2}O_2$ (henceforth NMTO) sodium layered oxide cathode by means of X-ray photoelectron spectroscopy (XPS) and correlated with the applied current density under battery operation. The Co- and Ni-free, and Mn-rich layered oxides have been recently enticed great attention as cathode materials for SIBs because they are made from Earth's crust abundant elements, remarkable electrochemical performance, which render them cost-competitive for SIBs.[33,34] Among Mn-rich layered oxides, the NMTO is particularly interesting because its chemical composition is based on Mn and Ti. The Mn is a non-toxic, abundant, and low-cost transition metal, which allows tuning the redox voltages owing to its multiple oxidation states.[34] In contrast, Ti doping increases the Na interlayer distance[35–38] and buffers the distortion of Jahn–Teller-active Mn^{III} providing better (de)insertion of Na^+ and structural reversibility upon cycling.[39,40] The crystal structure changes of this electroactive cathode material upon electrochemical cycling have been already studied,[41] including the aforementioned buffering of the Jahn–Teller distortions by means of Ti doping.[40]

2. Results and Discussion

2.1. Electrochemical Properties of P2-$Na_{0.67}Mn_{0.8}Ti_{0.2}O_2$ at Different Current Densities

The electrochemical cycling performance of NMTO has been investigated at current densities spanning over two orders of magnitude, i.e., 0.12 mA cm^{-2} (0.05 C), 0.21 mA cm^{-2} (0.01 C), 0.42 mA cm^{-2} (0.2 C), 2.12 mA cm^{-2} (1 C), and 10.6 mA cm^{-2} (5 C). Henceforth, the C rate nomenclature is used for an easier understanding.

The 1st, 2nd, 25th, 50th, 75th, and 100th voltage profiles are illustrated in **Figure 1**. NMTO displays a smooth voltage profile at all tested currents, with two short plateaus near 3.8 and 2.1 V vs Na/Na$^+$ appearing at low current densities, i.e., 0.05C, 0.1C, and 0.2C C rates. The low-voltage plateau is related to the redox reaction of Mn^{III}/Mn^{IV} (note that Ti^{IV} is electrochemically inactive in the studied voltage range), while the high-voltage plateau can be assigned to the phase transition from P2- to OP4-type.[41] In the initial cycles, NMTO shows a capacity fading at both the low- and high-voltage plateaus at low current densities (<1C), but the delivered capacity stabilizes upon further cycling. The irreversible capacity at high-voltage indicates that the P2-OP4 phase transition is not reversible. Meanwhile, the capacity loss at low-voltage is related to the disproportionation reaction of the Jahn–Teller-active Mn^{III},[42] forming Mn^{IV} and Mn^{II} species, with the latter dissolving into the carbonate-based electrolyte.[43] At higher current densities, namely 1C and 5C, the capacity loss at high- and low-voltage is negligible due to the kinetically limited occurrence of the high-voltage phase transition and Mn^{III} formation.

The cycling performance graph (Figure 1f) shows that, as expected, the delivered discharge capacity decreases upon increasing the applied current density. In the 2nd cycle, NMTO delivers a discharge capacity of 148.9, 127.2, 122.1, 84.8, and 45.9 mAh g^{-1} at 0.05, 0.1, 0.2, 1, and 5C, respectively. These results indicate that NMTO owns good rate performance delivering at 5C 50% of the capacity delivered at 0.1C. This suggests that NMTO exhibits fast Na$^+$ (de)intercalation kinetics similar to that of P2-$Na_{0.67}Mn_{0.8}Fe_{0.1}Ti_{0.1}O_2$.[41,44] The initial Coulombic efficiency (ICE) is also affected by the cycling speed. Indeed, cycling at current densities of 0.05, 0.1, 0.2, 1, and 5C result in ICE values of 54.2%, 59.2%, 62.9%, 79.3%, and 99.9%, respectively. This would be in agreement with electrolyte decomposition mainly occurring at low current densities. When considering the capacity retention after 100 cycles, using the capacity delivered at the 2nd as a reference, there is a remarkable increase from 91.7% at 0.05C to 96.5% at 0.1C and 96.0% at 0.2C. At higher C rates, namely 1 and 5C, the capacity retention increases even further (>100%—note that the capacity increases upon electrochemical cycling), which might be related to electrolyte wetting the electrode porosity and kinetics of the Na$^+$ (de)intercalation process.
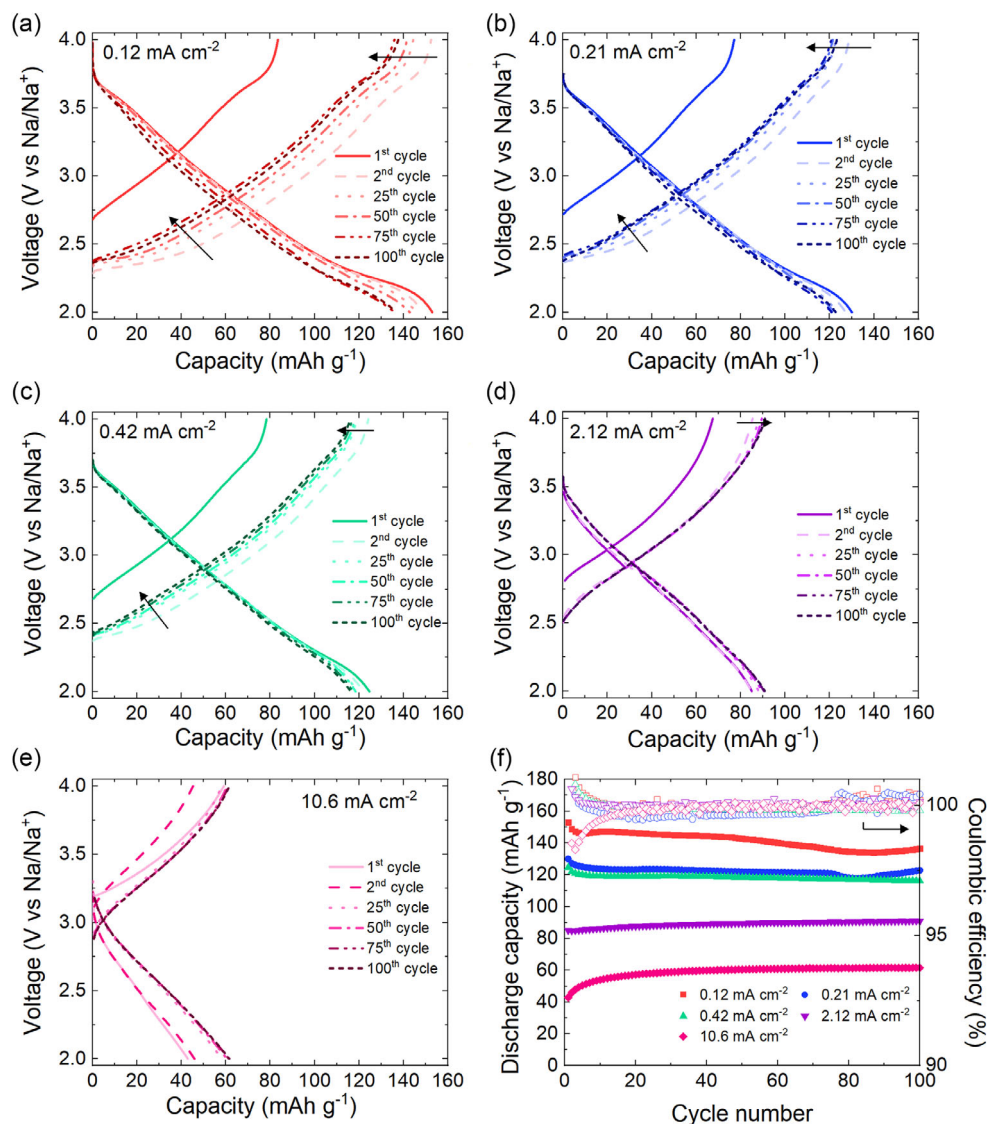
Figure 1. 1st, 2nd, 25th, 50th, 75th, and 100th voltage profiles of P2-Na$_{0.67}$Mn$_{0.8}$Ti$_{0.2}$O$_2$ electrodes at: a) 0.12 mA cm^{-2} (0.05C), b) 0.21 mA cm^{-2} (0.01C), c) 0.42 mA cm^{-2} (0.2C), d) 2.12 mA cm^{-2} (1C), and e) 10.6 mA cm^{-2} (5C) current densities. f) Cycling performance at 0.05C (red), 0.01C (blue), 0.2C (green), 1C (purple) and 5C (pink). All cells were cycled within the 2.0–4.0 V (vs Na/Na$^+$) range at 20 ± 2 °C.

2.2. CEI Properties at Different Current Densities

The CEI chemical composition and Mn oxidation state of NMTO electrodes tested at different current densities have been investigated by means of XPS. The Mn 2p, C 1s, F 1s, Na 1s, P 2p, and O 1s photoelectron lines have been collected to elucidate the influence of the applied current density on the chemical composition of the formed CEI, as well as on the Mn oxidation state.

2.2.1. Native Passivation Layer on P2-Na$_{0.67}$Mn$_{0.8}$Ti$_{0.2}$O$_2$ Pristine Electrode

First, the native passivation layer of the NMTO pristine electrode has been analyzed as a reference (**Figure 2**). It is known that the layered oxides are reactive to air/moisture

and hence a spontaneous thin surface layer is expected to form.[45] The native spontaneous passivation layer is rather thin, ≈ 5 nm, as determined by previous photoemission experiments on the grounds of Tanuma and coll. photoelectron inelastic mean free path (IMFP) estimation.[46] Indeed, the main peaks observed correspond to electrode components, i.e., the —C=C— bond from C65 conductive additive at 284.4 eV,[47] -CH$_2$ and -CF$_2$ groups from PVdF binder at 286.3 and 290.9 eV in the C 1s and 688.1 eV in the F 1s region,[48] as well as the peak corresponding to the metal–oxygen bond from NMTO observed in the O 1s spectrum at 530 eV.[35,36] In addition, the surface-sensitive Na 1s photoelectron region (note that the IMFP of Na 1s photoelectrons is very short) shows a low amount of carbonates (Na$_2$CO$_3$ and NaCO$_3$R), as well as NaF,[24] indicating once more the low thickness of the spontaneous native passivation layer.
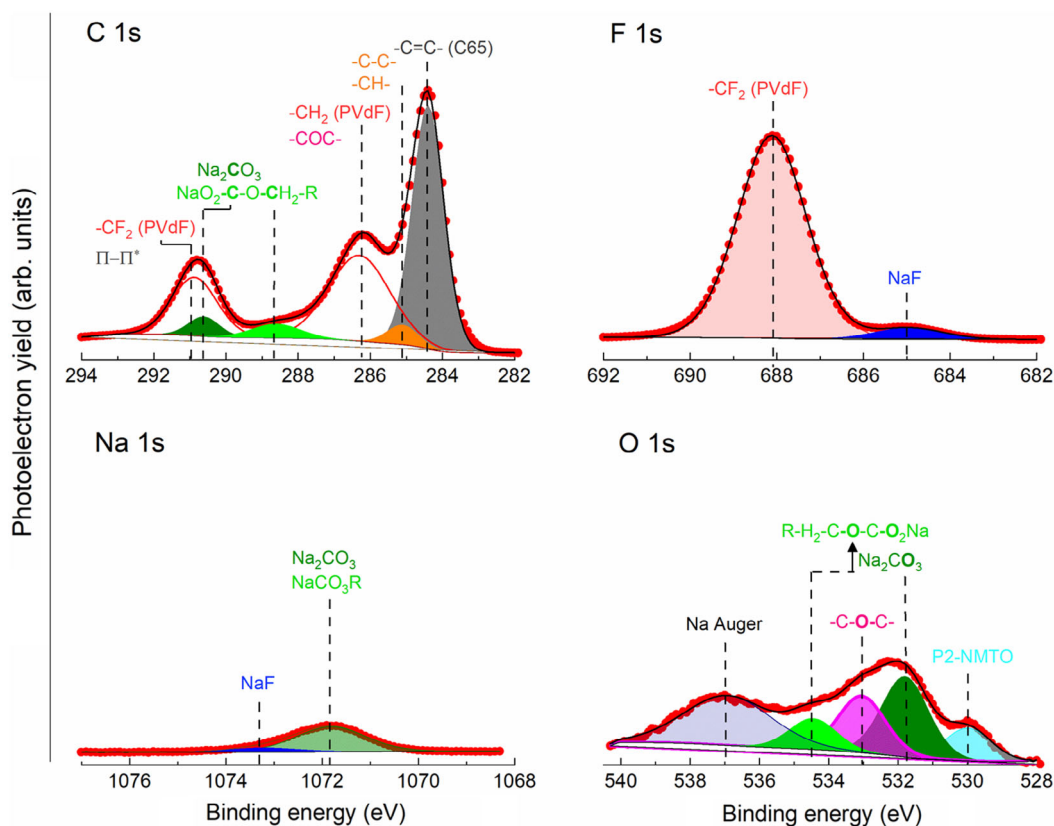
ADVANCED
SCIENCE NEWS
www.advancedsciencenews.com

Energy Technology
Generation, Conversion, Storage, Distribution
www.entechnol.de

Figure 2. C 1s, F 1s, Na 1s, and O 1s photoelectron lines of P2-$Na_{0.67}Mn_{0.8}Ti_{0.2}O_2$ pristine electrodes. Experimental data (red points) and peak fitting (colored areas) are also shown.

Nonetheless, a passivation layer is observed in the pristine electrode already, which is composed mainly of carbon–oxygen species, such as Na_2CO_3, $NaCO_3R$, and ethers (-COC-),[47,49] confirming the reactivity of the layered oxides toward air/moisture.[50] Also, a small amount of NaF is observed in the pristine electrodes (see F 1s at 684.9 eV and Na 1s at 1073.2 eV), indicating that small water traces in the electrode slurry result in high pH yielding to PVdF dehydrofluorination, i.e., decomposing the binder even before electrochemical cycling.[17,51,52] Overall, these results indicate that a thin spontaneous passivation surface layer is formed already during electrode preparation, which can undoubtedly influence the reactivity of the electrolyte under battery operation. In fact, the CEI will form on top of such a spontaneously formed (native) passivation layer and the electrolyte.

2.2.2. Mn Oxidation State and Chemical Composition of CEI of P2-$Na_{0.67}Mn_{0.8}Ti_{0.2}O_2$ at Different Current Densities

First, the Mn oxidation state on the surface of the cycled electrodes at different current densities, i.e., 0.05 and 5C, has been studied and compared with the oxidation state of Mn in the pristine electrode. Considering that Mn has six stable oxidation states, with three of them (2+, 3+, and 4+) displaying remarkable multiplet splitting, the fitting of the Mn $2p_{3/2}$ region when different oxidation states coexist is very challenging. In our case, we have

fitted the Mn $2p_{3/2}$ spectra following the fitting models described by Biesinger et al.,[53] as illustrated in Figure S1, Supporting Information. These models were developed on reference samples and, even there, five to six components are needed to reproduce the line shape of a reference pure sample with a single oxidation state. It is thus clear that the fitting of photoelectron lines where several oxidation states coexist is an exercise with a considerable intrinsic indetermination.

The results of the Mn $2p_{3/2}$ fitting of pristine electrode show that the Mn oxidation state is a mixture of Mn^{III} and Mn^{IV}. Note that pristine NMTO is only partially sodiated ($\approx$0.67 Na) and the Ti oxidation state is 4+, as confirmed by the XPS spectrum of the Ti 2p region (see Figure S2, Supporting Information) as well as by previous X-ray absorption (XANES) measurements that yield to the following material's stoichiometry, $Na_{0.67}Mn^{III}_{0.67}Mn^{IV}_{0.13}Ti^{IV}_{0.2}O_2$,[40] which corresponds to 84% of Mn^{III} and 16% of Mn^{IV}, i.e., in line with the experimental values obtained from the Mn $2p_{3/2}$ XPS fitting.

The cycled electrodes used for the XPS study were disassembled at the desodiated state of charge (4.0 V vs Na/Na^+), in theory corresponding to the full oxidation of Mn^{III} to Mn^{IV}. However, from the voltage profiles at the various current densities (see Figure 1), the sodium content (expressed as x in $Na_xMn_{0.8}Ti_{0.2}O_2$) corresponds to $\times \approx 0.2$ at 0.05C and $x \approx 0.54$ at 5C. These values suggest the presence of Mn^{III} traces in the desodiated electrodes, which is in agreement with the Mn

**ADVANCED
SCIENCE NEWS**

www.advancedsciencenews.com

Energy Technology
Generation, Conversion, Storage, Distribution

www.entechnol.de

$2p_{3/2}$ spectra recorded at the desodiated state (see Figure S1, Supporting Information) hinting at the presence of Mn^{III}. The determined amount of Mn^{III} is higher for the NMTO electrode desodiated at the highest current density, where the Na^+ insertion/extraction occurs to a lower extent due to kinetics reasons as confirmed by the delivered capacity values. Interestingly, the Mn $2p_{3/2}$ spectrum of the electrode cycled at 0.05C shows a distinctive shoulder toward higher binding energies (Figure S1 central panel, Supporting Information). This feature, occurring at >4 eV higher than the main Mn $2p_{3/2}$ peak, is the peculiar satellite peak of Mn^{II}, which is not seen for other oxidation states. The fitting of these satellite features is rather complex and not free of discussion, in fact, the intensity and position of the satellite peak depend, among other factors, on the local magnetic moment and the hybridization of the Mn 2p levels. It seems that very intense charge-transfer satellites shifted >4 eV from the main peak (Mn $2p_{3/2}$) can only be due to weak hybridizations in the surface.[54] Therefore, this indicates the formation of Mn^{II} during the discharge process, which dissolves in the carbonate-based electrolyte but is partially trapped in the CEI. Thus, the higher

capacity decay observed at 0.05C compared with electrodes cycled at higher current densities is to be related to the structure degradation occurring upon electrochemical cycling.

The evolution of the elemental composition of the CEI at different current densities was also determined by means of XPS (Figure S3, Supporting Information). This experiment clearly shows that the current density influences the chemical composition of the CEI. The carbonaceous species are mostly observed at high current densities and mainly correspond to the conductive carbon, as will be shown later. Meanwhile, fluorine-, oxygen- and phosphorus-based species are mostly formed at low current densities. These preliminary results suggest that the electrochemically driven electrolyte decomposition reactions, mainly related to the salt, become more pronounced when decreasing the current density.

The chemical composition of the formed CEI on NMTO electrodes subjected to different formation current densities has been also investigated by analyzing the C 1s, F 1s, Na 1s, and P 2p photoelectron lines, as illustrated in **Figure 3** and Table S1, Supporting Information, which the latter one collects
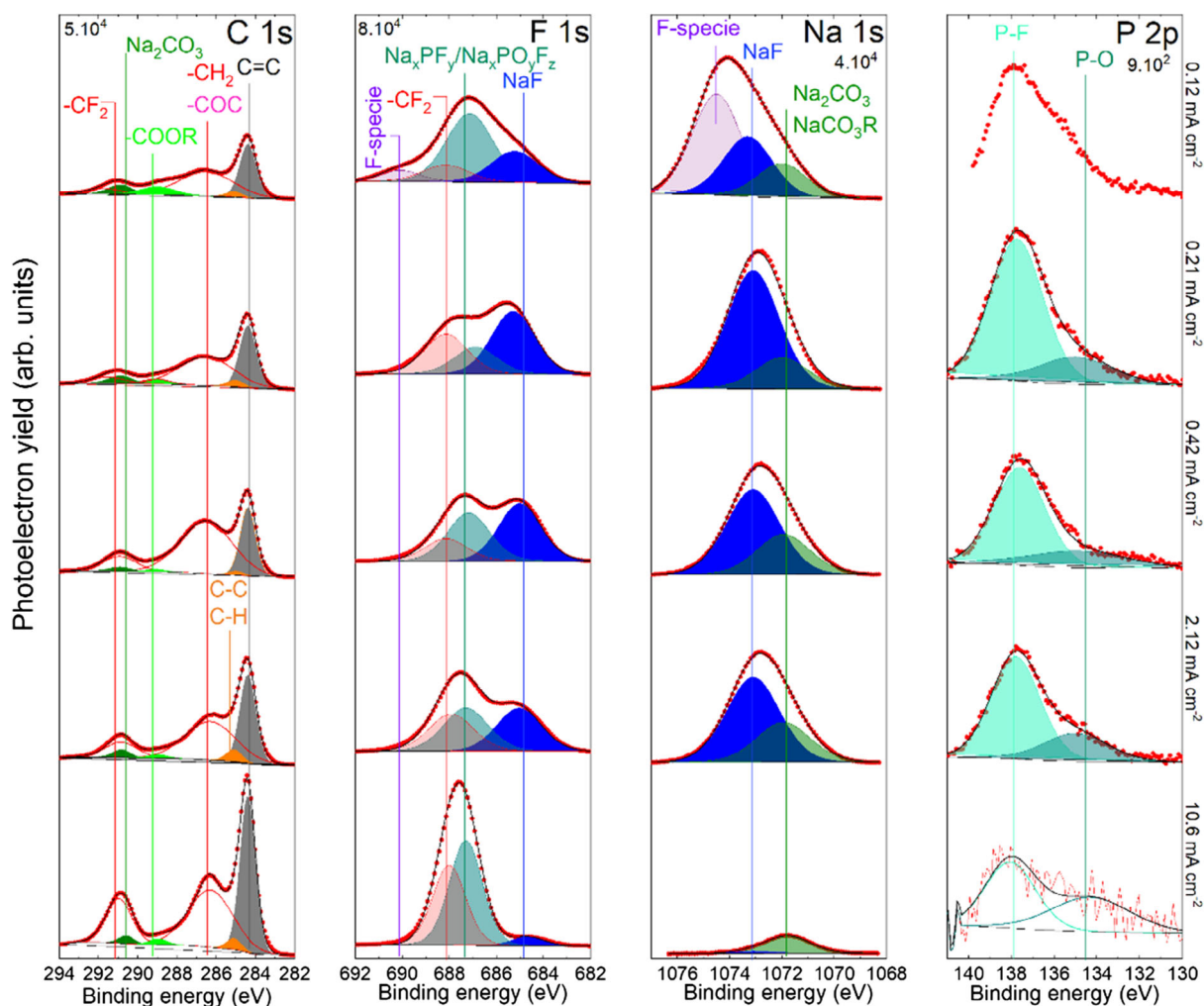

Figure 3. C 1s, F 1s, Na 1s, and P 2p photoelectron lines of P2-$Na_{0.67}Mn_{0.8}Ti_{0.2}O_2$ cycled electrodes at 0.12 mA cm^{-2} (0.05C), 0.21 mA cm^{-2} (0.1C), 0.42 mA cm^{-2} (0.2C), 2.12 mA cm^{-2} (1C), and 10.6 mA cm^{-2} (5C) (from top to bottom). The 1C rate current density corresponds to 265 mA g^{-1}.

**ADVANCED
SCIENCE NEWS**

www.advancedsciencenews.com

Energy Technology
Generation, Conversion, Storage, Distribution

www.entechnol.de

the concentration of observed species at different current densities. The analysis of the C 1s region reveals the —C=C— peak from C65 at 284.4 eV[47] and the —CH$_2$ peak at 286.3 eV and —CF$_2$ peak at 290.9 eV both from the PVdF binder[48] to reduce in intensity as current density decreases. In addition, the peaks of carbon-oxygen species, ascribed to CEI components, remain constant, indicating that the CEI is progressively thickening by reducing the current density. Indeed, the CEI is negligible at 5C, where only small concentrations of Na$_2$CO$_3$ and NaCO$_3$R are observed, mainly corresponding to the native passivation layer observed in the pristine electrode (see Section 2.2.1). In addition, the -CH$_2$ peak from PVdF is slightly shifted toward higher binding energies when reducing the current density. This could be due to the formation of ethers, note that the —COC— bond appears at similar binding energy than —CH$_2$—, overlapping with the —CH$_2$ peak from PVdF. This hypothesis is based on the fact that the decomposition of EC and PC by ring-opening and the following polymerization forms polymer compounds as polyethylene glycol (PEO).[27,55]

The F 1s photoelectron line agrees with the observations of the C 1s region. The intensity of the -CF$_2$ peak of PVdF at ≈688 eV decreases as the current density is reduced, suggesting once more the formation of a thicker CEI at lower current densities, while the opposite trend is observed for NaF (at 684.9 eV), which increases gradually. The NaF formation confirms the electrolyte decomposition by FEC reduction,[56,57] and NaPF$_6$ decomposition,[15,27] as well as the PVdF dehydrofluorination.[51] Nevertheless, the trend is interrupted at very low current density (i.e., 0.05C), where the main species (Na$_x$PF$_y$ or/and Na$_x$PO$_y$F$_z$ at 687 eV) correspond to the NaPF$_6$ decomposition reactions. Although the presence of salt traces on the surface cannot be excluded, the much higher Na$_x$PF$_y$/Na$_x$PO$_y$F$_z$ concentration at 0.05C might be related to the salt decomposition into fluorophosphates, in agreement with the slower kinetics of the decomposition reactions. Indeed, fluorophosphates have been already observed on layered oxide cathode electrodes cycled at low current density.[24,49] In addition, the extra peak toward higher binding energies (690.1 eV) might be related to the formed new species such as —CHF— and —CF$_2$-based compounds, but mainly including Na-modified -CF$_2$-groups, that are triggered by the dehydrofluorination of PVdF previously detected by ^{19}F-NMR.[17] Furthermore, in contrast with the observed concentration of carbon-based species, the fluorine-based ones are more abundant, suggesting a fluorine-rich CEI as otherwise expected considering the decomposition of fluorine-containing species, such as FEC, NaPF$_6$, and PVdF. The formation of a fluorine-rich CEI is also confirmed by the Na 1s photoelectron line showing that NaF (1073.3 eV) and F-species (1074.5 eV) (the latter ones only present when cycling at 0.05C) are present at a higher concentration than the carbon-based ones (Na$_2$CO$_3$/NaCO$_3$R at 1072 eV).[24] In addition, the Na 1s provides the scheme of the chemical composition of CEI. The low kinetic energy of Na 1s photoelectrons is translated in a short IMFP, thus revealing the chemical composition of the CEI outermost region. The absence of fluorine-based species and the reduced amounts of Na$_2$CO$_3$/NaCO$_3$R formed on the electrode cycled at 5C indicate, once more, that the CEI is rather thin at high current densities. It also confirms that, when reducing the current density, the electrolyte salt is mainly decomposed resulting in a fluorine-rich CEI.

In contrast, the P 2p photoelectrons provide the chemical composition of the subsurface region. In agreement with the observations of the Na 1s peak, the phosphates (P–O, at ≈135 eV) and fluorophosphates (P–F, at ≈138 eV) concentration increases at lower current densities.[58] These results point to a CEI mainly consisting of salt decomposition products, such as NaF, phosphates, and fluorophosphates, and displaying a depth profile with significant composition differences. It should be mentioned that there might be a slight cross-talk between the sodium metal counter electrode and the layered oxide electrode due to the high reactivity of sodium metal.[59,60] However, previous studies have confirmed that sodium metal does not affect the chemical composition of the interphase.[61]

Overall, the analysis of the XPS photoelectron lines indicates a thicker CEI forming by reducing the current density (for a better comparison see Table S2, Supporting Information). The thickness of the CEI has been estimated from Tanuma et al. photoelectron IMFP equation,[46] and considering the concentration of the —C=C— component (C65) of Table S1, Supporting Information. However, it should be considered that, in this case, the thickness of CEI is challenging to determine since the electrode is made of three different materials with different ionic and electronic conductivities, along with the complexity of CEI which is expected to have a heterogeneous distribution of inorganic and organic species.

In contrast, the almost negligible CEI formed at 5C is against the electrochemical nucleation and growth theory,[62] stating that high current densities lead to a large amount of small crystal nuclei on the electrode surface that allows for a high nucleation rate. Actually, it has been already experimentally observed that the electrochemical nucleation and growth theory is not followed for the SEI formation on graphite anodes.[62–65] These previous studies indicate that the transport properties of alkali ions affect the SEI/CEI formation, showing a poorer alkali ion transport upon increasing the current density. Hence, if the Na$^+$ transport is lower at high current densities, the electrochemically driven decomposition reactions of the electrolyte will be disrupted due to the low Na$^+$ concentration on the surface of the passive layer spontaneously formed upon the electrode-making process. In fact, the effect is more pronounced at high current density (5C), probably due to the lack of time to transport all the needed Na$^+$ to the interface.

2.2.3. Applied Current Density vs Operating Time: Influence on the CEI of P2-Na$_{0.67}$Mn$_{0.8}$Ti$_{0.2}$O$_2$

To elucidate if the observed influence of the current density on the CEI formation is due to the applied electron flux or to the overall operating time in the cells, an additional experiment was performed to evaluate the effect of immersion time in the electrolyte for electrodes tested at different C rates. In particular, a NMTO electrode was subjected to 120 cycles at 5C to achieve the overall cycling time of the electrode cycled at 0.1C for 10 cycles. The corresponding C 1s, F 1s, Na 1s, and P 2p photoelectron lines of the 5C cycled electrode over 120 cycles are illustrated in **Figure 4**. Regardless of the applied current density, the formed CEI is chemically similar but diverse in terms of species concentration. The —C=C— peak (at 284.4 eV) of C65 conductive
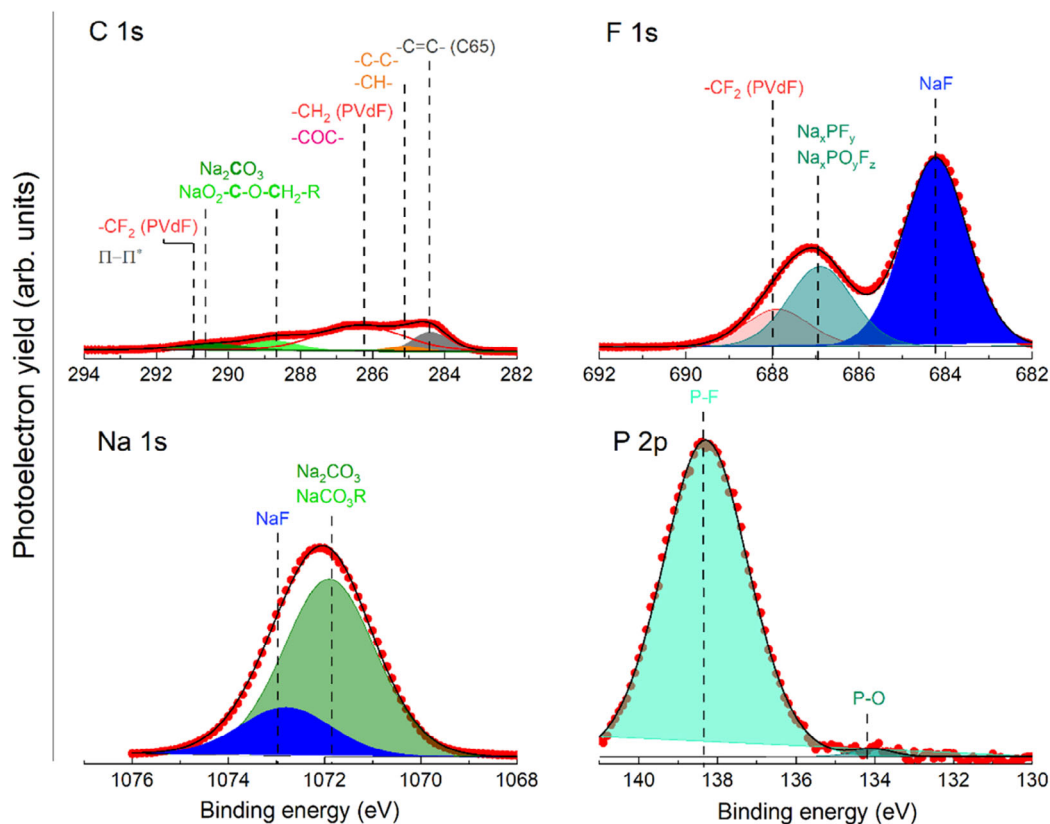
Figure 4. C 1s, F 1s, Na 1s, and P 2p photoelectron lines of P2-$Na_{0.67}Mn_{0.8}Ti_{0.2}O_2$ electrode cycled at 10.6 mA cm^{-2} (5C) over 120 cycles, which equals in cycling time to the P2-$Na_{0.67}Mn_{0.8}Ti_{0.2}O_2$ electrode cycled at 0.21 mA cm^{-2} (0.1C) over 10 cycles.

additive[47] in the NMTO electrode cycled at 5C over 120 cycles is much less pronounced (see Figure 4) than for the electrode cycled at 0.1C over 10 cycles (see Figure 3). Meanwhile, the peaks of the other electrode components, e.g., the —CH_2 (286.3 eV) and —CF_2 groups (290.9 and 688.1 eV, respectively, in the C 1s and F 1s regions)[48] of PVdF are rather similar. These results suggest that the electrolyte is decomposed to a larger extent over the conductive carbon, but not on the binder, although in the initial cycles at 5C no evidence of CEI formation is found (see Section 2.2.2). The surface of conductive carbon appears to be covered by Na_2CO_3 and $NaCO_3R$ in the outermost region, as indicated by the Na 1s region, and by NaF at higher depths (see F 1s). These results clearly show that the operating time also affects the thickness and properties of CEI. Considering that the Na$^+$ transport is less effective at high current densities, one possible explanation for the origin of the needed Na$^+$ ions contributing to the electrochemically driven electrolyte decomposition could be the electrode outermost surface region acting as Na$^+$ ions source. However, the confirmation of this hypothesis would need additional studies.

2.2.4. CEI Formation on P2-$Na_{0.67}Mn_{0.8}Ti_{0.2}O_2$ Electrode Operation at Realistic Conditions

The electrode–electrolyte interphases, i.e., SEI and CEI, are usually investigated at constant current density upon electrochemical cycling; being 0.1C as the most common C rate. However, the actual current density in the battery will depend on the application, for example, urban public transport usually requires a fast charge followed by a long discharge process.[66,67] To investigate the CEI evolution upon cycling at different charge and discharge current densities, the NMTO electrode has been set under fast charge and slow discharge C rates (1C/0.1C). The voltage profiles and the cycling performance (Figure S4, Supporting Information) show that the electrochemical properties of NMTO degrade more than at constant current, both in terms of delivered capacity and long-term stability. The NMTO delivers a discharge capacity of 94.7 mAh g^{-1} in the second cycle with a capacity retention of 83.1% over 100 cycles. The lower capacities, as well as lower stability, are due to the partial desodiation process (charge) owing to the high C rate (1C) that limits the further sodiation (discharge).

However, the decreased capacity retention might also arise from the active material degradation associated to the formation of soluble Mn^{II}. The analysis of the Mn 2p$_{3/2}$ peak confirms that Mn^{III} is not fully oxidized to Mn^{IV} because of the partial desodiation of NMTO at a high current density (**Figure 5**). In fact, the Mn 2p$_{3/2}$ peak fitting gives the following oxidation state concentrations: 72% Mn^{IV}, 12% Mn^{III}, and 16% Mn^{II}. The higher capacity fading observed when using a more realistic testing protocol than the conventional 1C (or 0.1C) charge and discharge C rate, might be related, on the one hand, to the desodiation
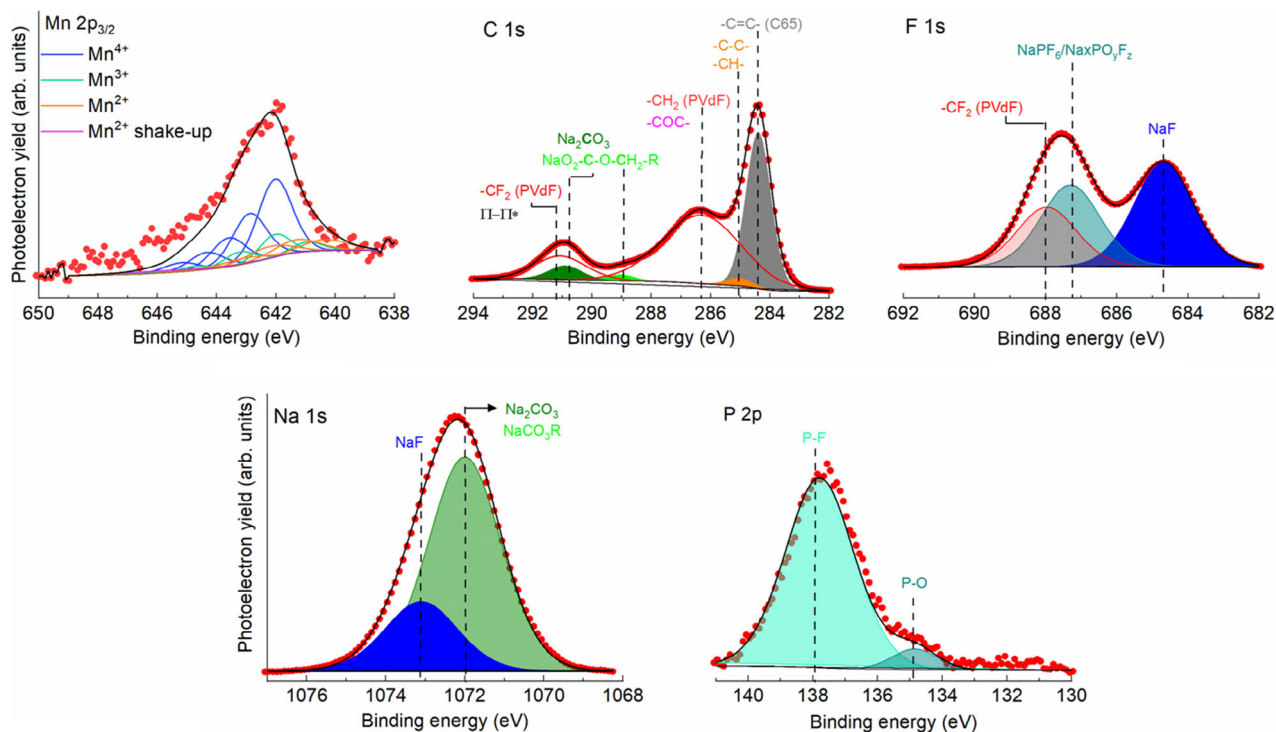
ADVANCED
SCIENCE NEWS
www.advancedsciencenews.com

Energy Technology
Generation, Conversion, Storage, Distribution
www.entechnol.de

Figure 5. Mn 2p$_{3/2}$, C 1s, F 1s, Na 1s, and P 2p photoelectron lines of P2-Na$_{0.67}$Mn$_{0.8}$Ti$_{0.2}$O$_2$ cycled electrode at 2.12 mA cm^{-2} (1C) and 0.21 mA cm^{-2} (0.1C) upon charge and discharge respectively over 10 cycles.

limitation (not fully desodiated as in 0.1C) and, on the other hand, to the formation of Mn^{II} upon sodiation, resulting from the structural degradation associated to the Jahn–Teller active Mn^{III}.[42]

In contrast, the characteristics of the CEI grown on the electrode subjected to the 1C/0.1C cycling protocol are rather similar in terms of chemical composition and thickness to those of electrode tested at 1C/1C, but not to those tested at 0.1C/0.1C in terms of CEI thickness. In fact, the chemical composition observed at 1C/0.1C is: 1) —COC— organic compound such as PEO due to the ring-opening and polymerization of EC and PC ($\approx$ 286.1 eV— C 1s);[27,55] 2) NaCO$_3$R (288.9 and 290.8 eV—C 1s; 1072.0 eV Na 1s) and Na$_2$CO$_3$ (290.8 eV—C 1s; 1072.0 eV—Na 1s) due to the EC–PC reduction,[54] 3) Na$_x$PF$_y$ and Na$_x$PO$_y$F$_z$ (687 eV—F 1s; $\approx$135 and $\approx$138 eV—P 2p) due to the NaFP$_6$ decomposition reactions,[17,27] and 4) NaF (684.9 eV—F 1s; and 1073.2 eV—Na 1s) owing to FEC reduction,[56,57] NaPF$_6$ decomposition[15,27] and PVdF dehydrofluorination.[51,52] Nevertheless, the concentration of the species differs from the CEIs formed on NMTO electrodes at 5 and 0.1C. In particular, the NaF concentration from the F 1s region is found to be similar as for the electrode cycled at 0.1C/0.1C, while the Na 1s spectrum shows that the main peak corresponds to carbonates (NaCO$_3$R/ Na$_2$CO$_3$), i.e., as for the electrode cycled at 5C. This suggests that the reduction of FEC and NaPF$_6$ salt, as well as the PVdF dehydrofluorination, occur first, forming NaF close to the electrode surface. Following, the EC and PC reduction reactions occur, hence the CEI shows a carbonate-rich outermost layer. As discussed earlier, the higher concentration of carbonates in the outermost region is

ascribed to the high current density upon charge that hinders the Na$_2$CO$_3$/NaCO$_3$R dissolution while showing a large concentration of them upon charge. It should be considered that these species (Na$_2$CO$_3$/NaCO$_3$R) are mainly formed during the discharge and partially dissolved during the charge because of their high solubility in carbonate-based electrolyte.[17,30] Therefore, these results confirmed once more that the applied current density is a key parameter on the electrode–electrolyte interphase formation, as well as for tuning the composition and thickness of the SIB interphases.

3. Conclusions

The electrochemical performance of P2-Na$_{0.67}$Mn$_{0.8}$TiO$_2$ employed as cathode for SIBs has been characterized at different current densities as well as charge/discharge protocols, showing excellent C rate capability in all cases. The analysis of the electrochemical performance has included the evaluation of the CEI evolution and its influence on electrochemical performance. The analysis of the pristine electrode interphase shows that a spontaneous carbonate-rich passivation layer is already formed during the electrode-making process. Although the resulting electrodes show good C rate capability, such a passive layer influences the subsequent electrode–electrolyte interphase formation. To understand the CEI evolution, its composition upon electrochemical cycling has been probed at different current densities by means of XPS, thus correlating the CEI properties with the applied current density. As a result, it has been found that the species of the CEI do not change with current density, being

**ADVANCED
SCIENCE NEWS**

www.advancedsciencenews.com

Energy Technology
Generation, Conversion, Storage, Distribution

www.entechnol.de

NaF-rich species the main components. In stark contrast, the species concentration and the thickness of the CEI are strongly affected by the current density and the operating time. A thicker CEI can be formed in two ways, first, by reducing the current density and, second, by increasing the operation time at high current densities. The latter protocol allows forming a time–cost-efficient good passivation CEI, as suggested by the results obtained at 5C and higher operating time. In addition, these results indicate that not only the electrode–electrolyte composition is critical for the CEI formation, but all the electrochemical cycling parameters should be considered, such as the applied current density, temperature, operation time, working voltage window, etc. At the same time, the time- and cost-consuming CEI formation process could be reduced by applying high current densities and varying the operation time until the most suitable electrode–electrolyte interphase is formed. Ultimately, this would have a positive impact on the fabrication costs of battery manufacturers.

4. Experimental Section

Synthesis of P2- Sodium Manganese-Rich Layered Oxide: P2-$Na_{0.67}Mn_{0.8}Ti_{0.2}O_2$ (NMTO) was synthesized by solid-state method, mixing in a stoichiometric amount anhydrous sodium carbonate (Na_2CO_3, 99.8%, Sharlab), manganese (III) oxide (Mn_2O_3, 98%, Alfa Aesar), and anatase titanium (IV) oxide (TiO_2, 99.6%, Alfa Aesar) in a mortar until a homogeneous brown powder is obtained. The resultant powder was pelletized and annealed up to 1000 °C under atmospheric conditions for 10 h. The obtained sample was transferred to an Ar-filled glove box to avoid contact with the atmosphere.[36]

Structural Characterization of P2- Sodium Manganese-Rich Layered Oxide: The purity of the NMTO phase has been confirmed by powder X-ray diffraction recorded on a Bruker Discover D8 instrument equipped with an LYNXEYE-XE detector, and monochromatic Cu radiation ($K\alpha_1 = 1.5406$ Å) with a step size of 0.02°. Le Bail refined with the FullProf software and the XRD pattern is illustrated in Figure S5, Supporting Information.[68]

Electrochemical Characterization: Electrodes were prepared by mixing NMTO active material, carbon Super C65 (Timcal C-Nergy-) and polyvinylidene fluorine (PVdF, Solef, Arkema Group) dissolved in *N*-methyl-2-pyrrolidone (NMP, Sigma Aldrich) in 80:10:10 ratio, respectively. The slurry was cast on battery-grade aluminum foil and dried at 120 °C under vacuum overnight. 12 mm electrodes were pressed at 5 tons for 30 s before assembling CR2032 coin cells in an Ar-filled glove box (MBraun, H_2O, and $O_2 < 1$ ppm). The coin cells were assembled using NMTO electrodes as the working electrode and metallic sodium disk (99.8%, Across Organics) as a counter electrode, glass fiber (Whatan GF/D) as a separator, and 1 M $NaPF_6$ (battery grade, FluoroChem) in EC: PC (in a 1:1 wt% (ethylene carbonate: propylene carbonate—battery grade, UBE) as electrolyte. The galvanostatic tests were carried out in a Maccor Series 4000 battery tested in the operating voltage window of 2.0–4.0 V vs Na/Na$^+$ at five different current densities: 0.12 mA cm^{-2} = 12.14 mA g^{-1} (0.05C), 0.21 mA cm^{-2} = 24.30 mA g^{-1} (0.01C), 0.42 mA cm^{-2} = 49.29 mA g^{-1} (0.2C), 2.12 mA cm^{-2} = 242.08 mA g^{-1} (1C), and 10.60 mA cm^{-2} = 1214.86 mA g^{-1} (5C), considering 1C = 265 mA g^{-1}, which corresponds to the theoretic exchange of one Na$^+$. Additionally, some of the coin cells were cycled at 2.12 mA cm^{-2} (1C) for the charging process and at 0.21 mA cm^{-2} (0.01 C) for discharge. The amount of electrolyte used was 100 μL and the mass loading of electrodes ≈2-3 mg cm^{-2}.

CEI Characterization: The CEI was investigated by means of XPS using a Phoibos 150 spectrometer (Specs GmbH) and monochromatic Al Kα ($h\nu = 1487$ eV) X-ray source. The XPS experiments were carried out on pristine electrode as reference and in cycled electrodes after 10th cycle at different current densities, i.e., 0.12 mA cm^{-2} (0.05C), 0.21 mA cm^{-2} (0.01C), 0.42 mA cm^{-2} (0.2C), 2.12 mA cm^{-2} (1C), and 10.60 mA cm^{-2} (5C), and 2.12 mA cm^{-2} (1C)/0.21 mA cm^{-2} (0.01C)

(charge/discharge respectively). In addition, extra cycled electrodes were studied, which was cycled the same time as the electrode cycled at 0.21 mA cm^{-2} (0.01C), but applying a higher current density (10.60 mA cm^{-2}—5C). The cycled electrodes were stopped after the 10th cycle, disassembled inside the Ar-filled glove box (MBraun, H_2O, and $O_2 < 1$ ppm), and rinsed with DMC (dimethyl carbonate, battery grade, UBE) and dried in the glove box pre-chamber before being transferred to the XPS vacuum chamber by an Ar-filled transfer system (never exposing the electrodes to air/moisture). High-resolution scans at low potential were acquired at 200 W, 30 eV pass energy, and 0.1 eV energy step. The CEI chemical composition was followed by analyzing the C 1s, F 1s, Na 1s, O 1s, and P 2p photoemission lines. The Ti and Mn transition metals evolution has also been studied by Ti 2p and Mn 2p photoemission regions. Calibration of the binding energy was carried out using the C 1s graphitic signal (—C=C—) as a reference at 284.4 eV.[69] The recorded spectra were fitted by CasaXPS software using a nonlinear Shirley-type background and a Voigt profile (70% Gaussian and 30% Lorentzian).[70]

Supporting Information

Supporting Information is available from the Wiley Online Library or from the author.

Conflict of Interest

The authors declare no conflict of interest.

Data Availability Statement

Research data are not shared.

[1] I. Hasa, S. Mariyappan, D. Saurel, P. Adelhelm, A. Y. Koposov, C. Masquelier, L. Croguennec, M. Casas-Cabanas, *J. Power Sources* **2021**, *482*, 228872.

[2] S. Kuze, J. Kageura, S. Matsumoto, T. Nakayama, M. Makidera, M. Saka, T. Yamaguchi, T. Yamamoto, K. Nakane, *Development of a Sodium Ion Secondary Battery, R&D Report, "Sumitomo Kagau"*, Sumitomo Chemical Co., Ltd. **2013**.

[3] L. Wang, J. Song, R. Qiao, L. A. Wray, M. A. Hossain, Y. De Chuang, W. Yang, Y. Lu, D. Evans, J. J. Lee, S. Vail, X. Zhao, M. Nishijima, S. Kakimoto, J. B. Goodenough, *J. Am. Chem. Soc.* **2015**, *137*, 2548.

[4] A. Bauer, J. Song, S. Vail, W. Pan, J. Barker, Y. Lu, *Adv. Energy Mater.* **2018**, *8*, 1.

[5] Y. Li, Y. S. Hu, X. Qi, X. Rong, H. Li, X. Huang, L. Chen, *Energy Storage Mater.* **2016**, *5*, 191.

[6] G. C. Congress, *Faradion Receives First Order for Sodium-Ion Batteries for Australian Market*, (accessed: April 2020).

[7] CATL, *CATL Unveils Its Latest Breakthrough Technology by Releasing Its First Generation of Sodium-ion Batteries*, (accessed: July 2021).

[8] M. A. Muñoz-Márquez, D. Saurel, J. L. Gómez-Cámer, M. Casas-Cabanas, E. Castillo-Martínez, T. Rojo, *Adv. Energy Mater.* **2017**, *7*, 1700463.

[9] C. Vaalma, D. Buchholz, M. Weil, S. Passerini, *Nat. Rev. Mater.* **2018**, *3*, 18013.

[10] E. Peled, *J. Electrochem. Soc.* **2006**, *126*, 2047.

[11] K. Edström, T. Gustafsson, J. O. Thomas, *Electrochim. Acta* **2004**, *50*, 397.

[12] R. Fong, U. von Sacken, J. R. Dahn, *J. Electrochem. Soc.* **1990**, *137*, 2009.

[13] J. Asenbauer, T. Eisenmann, M. Kuenzel, A. Kazzazi, Z. Chen, D. Bresser, *Sustain. Energy Fuels* **2020**, *4*, 5387.

[14] S. Komaba, W. Murata, T. Ishikawa, N. Yabuuchi, T. Ozeki, T. Nakayama, A. Ogata, K. Gotoh, K. Fujiware, *Adv. Funct. Mater.* **2011**, *11*, 3859.

[15] M. Dahbi, T. Nakano, N. Yabuuchi, S. Fujimura, K. Chihara, K. Kubota, J. Y. Son, Y. T. Cui, H. Oji, S. Komaba, *ChemElectroChem* **2016**, *3*, 1856.

[16] J. Fondard, E. Irisarri, C. Courréges, M. R. Palacin, A. Ponrouch, R. Dedryvère, *J. Electrochem. Soc.* **2020**, *167*, 070526.

[17] M. A. Muñoz-Márquez, M. Zarrabeitia, E. Castillo-Martínez, A. Eguía-Barrio, T. Rojo, M. Casas-Cabanas, *ACS Appl. Mater. Interfaces* **2015**, *7*, 7801.

[18] H. Moon, M. Zarrabeitia, E. Frank, O. Böse, M. Enterria, D. Saurel, I. Hasa, S. Passerini, *Batteries Supercaps* **2021**, *4*, 1.

[19] L. Baggeto, P. Ganesh, R. P. Meisner, R. R. Unoic, J. C. Jumas, C. A. Bridges, G. M. Veith, *J. Power Sources* **2013**, *234*, 48.

[20] L. Bodenes, A. Darwiche, L. Monconduit, H. Martinez, *J. Power Sources* **2015**, *273*, 14.

[21] L. Ji, M. Gu, Y. Shao, X. Li, M. H. Engelhard, B. W. Arey, W. Wang, Z. Nie, J. Xiao, C. Wang, J. G. Zhang, J. Liu, *Adv. Mater.* **2014**, *26*, 2901.

[22] L. Baggetto, E. Allcorn, A. Manthiram, G. M. Veith, *Electrochem. Commun.* **2013**, *27*, 168.

[23] M. Galceran, J. Rikarte, M. Zarrabeitia, M. C. Pujol, M. Aguiló, M. Casas-Cabanas, *ACS Appl. Energy Mater.* **2019**, *2*, 1923.

[24] S. Doubaji, B. Philippe, I. Saadoune, M. Gorgoi, T. Gustafsson, A. Solhy, M. Valvo, K. Edström, *ChemSusChem* **2016**, *9*, 97.

[25] L. Mu, X. Feng, R. Kou, Y. Zhang, H. Guo, C. Tian, C. J. Sun, X. W. Du, D. Nordlund, H. Li, F. Lin, *Adv Energy Mater.* **2018**, *8*, 1801975.

[26] I. Moeez, D. Susanto, W. Chang, H. D. Lim, K. Y. Chung, *Chem. Eng. J.* **2021**, *425*, 130547.

[27] M. Zarrabeitia, M. Casas-Cabanas, M. Á. Muñoz-Márquez, *Electrochim. Acta* **2021**, *372*, 137846.

[28] J. Song, B. Xiao, Y. Lin, K. Xu, X. Li, *Adv. Energy Mater.* **2018**, *8*, 1.

[29] M. A. Muñoz-Márquez, M. Zarrabeitia, S. Passerini, T. Rojo, *Adv. Mater. Interfaces* **2022**, 2101773.

[30] R. Mogensen, D. Brandell, R. Younesi, *ACS Energy Lett.* **2016**, *1*, 1173.

[31] X. Dou, I. Hasa, M. Hekmatfar, T. Diemant, R. J. Behm, D. Buchholz, S. Passerini, *ChemSusChem* **2017**, *10*, 2668.

[32] P. A. Nelson, K. G. Gallagher, I. D. Bloom, D. W. Dennis, *Modeling The Performance And Cost Of Lithium-Ion Batteries For Electric-Drive Vehicles*, 2nd edn., Chemical Sciences and Engineering Division, Argonne National Laboratory, United States **2012**. https://doi.org/10.2172/1209682.

[33] E. Gonzalo, M. Zarrabeitia, N. E. Drewett, J. M. López del Amo, T. Rojo, *Energy Storage Mater.* **2021**, *34*, 682.

[34] J. F. Peters, M. Baumann, J. R. Binder, M. Weil, *Sustain. Energy Fuels* **2021**, *5*, 6414.

[35] J. K. Park, G. G. Park, H. H. Kwak, S. T. Hong, J. W. Lee, *ACS Omega* **2017**, *3*, 361.

[36] P. F. Wang, H. R. Yao, X. Y. Liu, J. N. Zhang, L. Gu, X. Q. Yu, Y. X. Yin, Y. G. Guo, *Adv. Mater.* **2017**, *29*, 1700210.

[37] Z.-Y. Li, R. Gao, L. Sun, Z. Hu, X. Liu, *J. Mater. Chem. A* **2015**, *3*, 16272.

[38] H. Yoshida, N. Yabuuchi, K. Kubota, I. Ikeuchi, A. Garsuch, M. Schulz-Dobrick, S. Komaba, *Chem. Commun.* **2014**, *50*, 3677.

[39] Y. Wang, J. Liu, B. Lee, R. Qiao, Z. Yang, S. Xu, X. Yu, L. Gu, Y.-S. Hu, W. Yang, K. Kang, H. Li, X.-Q. Yang, L. Chen, X. Huang, *Nat. Commun.* **2015**, *6*, 6401.

[40] M. Zarrabeitia, E. Gonzalo, M. Pasqualini, M. Ciambezi, O. Lakuntza, F. Nobili, A. Trapananti, A. Di Cicco, G. Aquilanti, N. A. Katcho, J. M. López Del Amo, J. Carrasco, M. Á. Muñoz-Márquez, T. Rojo, *J. Mater. Chem. A* **2019**, *7*, 14169.

[41] M. H. Han, E. Gonzalo, N. Sharma, J. M. López Del Amo, M. Armand, M. Avdeev, J. J. Saiz Garitaonandia, T. Rojo, *Chem. Mater.* **2016**, *28*, 106.

[42] M. M. Thackeray, *Prog. Solid State Chem.* **1997**, *25*, 1.

[43] L. G. Chagas, D. Buchholz, L. Wu, B. Vortmann, S. Passerini, *J. Power Sources* **2014**, *247*, 377.

[44] A. J. Fernández-Ropero, M. Zarrabeitia, G. Baraldi, M. Echeverria, T. Rojo, M. Armand, D. Shanmukaraj, *ACS Appl. Mater. Interfaces* **2021**, *13*, 11814.

[45] M. H. Han, N. Sharma, E. Gonzalo, J. C. Pramudita, H. E. A. Brand, J. M. López Del Amo, T. Rojo, *J. Mater. Chem. A* **2016**, *4*, 18963.

[46] S. Tanuma, C. J. Powell, D. R. Penn, *Surf. Interface Anal.* **2011**, *43*, 689.

[47] R. I. R. Blyth, H. Buqa, F. P. Netzer, M. G. Ramsey, J. O. Besenhard, P. Golob, M. Winter, *Appl. Surf. Sci.* **2000**, *167*, 99.

[48] G. Beamson, D. Briggs, *High Resolution XPS of Organic Polymers. The Scienta ESCA300 Database*, John Wiley & Sons, Chichester, UK **1992**.

[49] M. Zarrabeitia, L. Gomes Chagas, M. Kuenzel, E. Gonzalo, T. Rojo, S. Passerini, M. Á. Muñoz-Márquez, *ACS Appl. Mater. Interfaces* **2019**, *11*, 28885.

[50] W. Zuo, J. Qiu, X. Liu, F. Ren, H. Liu, H. He, C. Luo, J. Li, G. F. Ortiz, H. Duan, J. Liu, M. S. Wang, Y. Li, R. Fu, Y. Yang, *Nat. Commun.* **2020**, *11*, 1.

[51] R. Crowe, J. P. S. Badyal, *J. Chem. Soc. Chem. Commun.* **1991**, 958.

[52] K. Kubota, S. Kumakura, Y. Yoda, K. Kuroki, S. Komaba, *Adv. Energy Mater.* **2018**, *8*, 1.

[53] M. C. Biesinger, B. P. Payne, A. P. Grosvenor, L. W. M. Lau, A. R. Gerson, R. S. C. Smart, *Appl. Surf. Sci.* **2011**, *257*, 2717.

[54] A. K. Shukla, P. Krüger, R. S. Dhaka, D. I. Sayago, K. Horn, S. R. Barman, *Phys. Rev. B* **2007**, *75*, 235419.

[55] A. M. Andersson, A. Henningson, H. Siegbahn, U. Jansson, K. Edström, *J. Power Sources* **2003**, *119–121*, 522.

[56] H. Kumar, E. Detsi, D. P. Abraham, V. B. Shenoy, *Chem. Mater.* **2016**, *28*, 8930.

[57] Q. Liu, D. Mu, B. Wu, L. Wang, L. Gai, F. Wu, *ChemSusChem* **2017**, *10*, 786.

[58] S. Malmgren, K. Ciosek, M. Hahlin, T. Gustafsson, M. Gorgoi, H. Rensmo, K. Edström, *Electrochim. Acta* **2013**, *97*, 23.

[59] D. I. Iermakova, R. Dugas, M. R. Palacín, A. Ponrouch, *J. Electrochem. Soc.* **2015**, *162*, A7060.

[60] J. Conder, C. Villevieille, *Chem Commun.* **2019**, *55*, 1275.

[61] M. Zarrabeitia, M. A. Muñoz-Márquez, F. Nobili, T. Rojo, M. Casas-Cabanas, *Batteries* **2017**, *3*, 16.

[62] E. Budevski, G. Staikov, W. J. Lorenz, *Electrochim. Acta* **2000**, *45*, 2559.

[63] S. Kranz, T. Kranz, T. Graubner, Y. Yusim, L. Hellweg, B. Roling, *Batter. Supercaps* **2019**, *2*, 1026.

[64] S. Bhattacharya, A. T. Alpas, *Carbon N. Y.* **2012**, *50*, 5359.

[65] S. Bhattacharya, A. R. Riahi, A. T. Alpas, *Mater. Res. Soc. Symp. Proc.* **2011**, *1388*, 20.

[66] P. Keil, A. Jossen, *J. Energy Storage* **2016**, *6*, 125.

[67] J. Brady, M. O'Mahony, *Sustain. Cities. Soc.* **2016**, *26*, 203.

[68] J. Rodríguez-Carvajal, *Phys. B Phys. Condens. Matter* **1993**, *192*, 55.

[69] C. D. Wagner, W. M. Riggs, L. E. Davis, J. F. Moulder, G. E. Muilenberg, in *Handbook of X-Ray Photoelectron Spectroscopy*, Perkin-Elmer Corporation, Physical Electronics Division, Minnesota, USA **1979**.

[70] J. Walton, P. Wincott, N. Fairley, A. Carrick, in *Peak Fitting with CasaXPS: A Casa Pocket Book*, Knutsford, UK **2010**.